Simulating hyperelastic materials with anisotropic stiffness models in a particle-based framework

Wang, Tiancheng; Xu, Yanrui; Li, Ruolan; Wang, Haoping; Xiong, Yuege; Wang, Xiaokun

Published in:
Computers and Graphics (Pergamon)

DOI:
10.1016/j.cag.2023.09.007

Computers & Graphics 116 (2023) 437–447

Contents lists available at ScienceDirect

Computers & Graphics

journal homepage: www.elsevier.com/locate/cag

Special Section on AniNex 2023

Simulating hyperelastic materials with anisotropic stiffness models in a particle-based framework

Tiancheng Wang [b,1], Yanrui Xu [b,c,1], Ruolan Li [b], Haoping Wang [b], Yuege Xiong [b], Xiaokun Wang [a,b,d,e,*]

[a] Beijing Advanced Innovation Center for Materials Genome Engineering, University of Science and Technology Beijing, Beijing, 100083, China
[b] School of Intelligence Science and Technology, University of Science and Technology Beijing, Beijing, 100083, China
[c] Bernoulli Institute for Mathematics, Computer Science and Artificial Intelligence, University of Groningen, Groningen, 9747 AG, the Netherlands
[d] Bournemouth University, Fern Barrow, Poole, Dorset, BH12 5BB, United Kingdom
[e] Key Laboratory of Intelligent Bionic Unmanned Systems, Ministry of Education, University of Science and Technology, Beijing, 100083, China

A R T I C L E   I N F O

Article history:
Received 29 June 2023
Received in revised form 17 August 2023
Accepted 14 September 2023
Available online 18 September 2023

Keywords:
Physically-based animation
Particle systems
Elastic simulation
Smoothed particle hydrodynamics

A B S T R A C T

We present a particle-based smoothed particle hydrodynamics (SPH) framework for simulating hyperelastic materials with anisotropic stiffness models. While most elastic simulations predominantly rely on mesh-based approaches, such as the Finite Element method, the relationship between Lamé's first parameter and Poisson's ratio complicates the strict enforcement of volume conservation, making it challenging to stabilize simulations for common biological tissues like fat and muscle. In this paper, we couple an implicit divergence-free SPH solver with particle-based deformation gradient computation and apply various elastic energy functions to achieve incompressible elastic simulations. The incompressibility of elastic objects and collisions between different bodies are managed by the implicit SPH algorithm. We further incorporate anisotropic energy functions, constructed from the extrapolation of Cauchy–Green invariants, to introduce anisotropic properties to the objects. By integrating activation and contraction coefficients into the energy functions, particles can simulate muscle contractions and lift heavy objects. Our method can effectively represent elastic objects with varying mechanical properties across different directions and be further employed to mimic muscle contractions. Experiments demonstrate that our approach provides realistic simulations for a wide range of animal and human body movements.

1. Introduction

The simulation of hyperelastic materials is of paramount importance in the field of computer graphics, with applications spanning various domains such as virtual surgery [1], soft robotics [2], and the study of biological tissues [3]. Over the years, numerous discretization methods have been utilized to study these materials, with mesh-based techniques such as the Finite Element Method (FEM) dominating the research landscape [4]. FEM has been favored due to its accuracy, ability to handle complex geometries, and compatibility with a wide range of material models. However, in recent years, particle-based methods like Smoothed Particle Hydrodynamics (SPH) have garnered increasing attention as an alternative to mesh-based techniques [5]. This growing interest is attributed to several factors, including the versatility of SPH in handling a diverse range of material properties, its ease of coupling with other simulation techniques, and the inherent guarantees of incompressibility it provides [6]. Additionally, particle-based methods offer unique advantages in terms of computational efficiency and scalability, making them well-suited for complex applications and large-scale simulations [7].

Particle-based methods offer several advantages compared to their mesh-based counterparts. Among these benefits is the ability to handle large deformations and topology changes more naturally, the absence of mesh distortion and element inversion issues, and the potential for efficient parallelization. Thanks to the study of simulating incompressible fluid using particles, SPH now can be applied to handle strongly incompressible elastic objects with existing elastic energy functions. And since each particle carries a certain portion of mass of the whole object, the Piola–Kirchhoff stress tensor of the energy models can be directly applied to computing the motion of the objects without

* Correspondence to: 30 Xueyuan Road, Haidian District, Beijing 100083, China.
E-mail addresses: m202121492@xs.ustb.edu.cn (T. Wang), yanrui.xu@rug.nl (Y. Xu), m202310601@xs.ustb.edu.cn (R. Li), m202210592@xs.ustb.edu.cn (H. Wang), m202210668@xs.ustb.edu.cn (Y. Xiong), wangxiaokun@ustb.edu.cn (X. Wang).
1 Co-first author.

https://doi.org/10.1016/j.cag.2023.09.007
0097-8493/

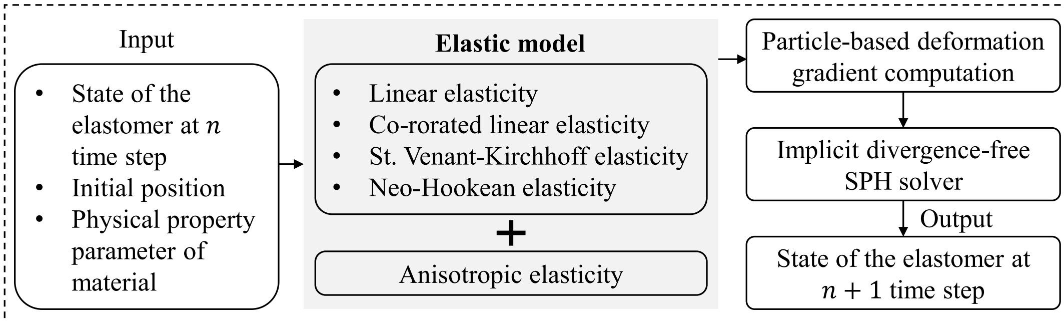

Fig. 1. SPH framework for simulating hyperelastic materials with anisotropic stiffness model.

the need of the Hessian matrices [8]. Consequently, numerous successful particle-based elastic simulation research endeavors have emerged.

Despite these advancements, there is a noticeable lack of anisotropic elastic simulation studies in particle-based methods. Anisotropic materials exhibit different mechanical properties depending on the direction in which they are measured, as opposed to isotropic materials, which have uniform properties in all directions [9]. This anisotropic behavior is commonly observed in various materials encountered in daily life, such as wood, which exhibits varying stiffness along and perpendicular to the grain, and composite materials like carbon fiber, where the arrangement of fibers influences the mechanical properties. Anisotropic materials are also found in biological tissues, such as muscles, tendons, and cartilage, which possess distinct stiffness characteristics along their primary axes due to their underlying fibrous structures [10]. Accurate simulation of anisotropic materials is of paramount importance in computer graphics, as it enables the creation of more realistic and lifelike virtual environments, objects, and characters. This is especially relevant in applications like medical simulation, where accurate representation of biological tissues is essential for effective training and planning of surgical procedures, as well as in the entertainment industry, where realistic animations contribute significantly to the overall visual experience. Given the prevalence of anisotropic materials in daily life and their significance in various applications, there is a pressing need to develop effective particle-based methods for anisotropic elastic simulation. By addressing this gap in the research landscape, we can pave the way for more accurate and realistic simulations of a wide range of materials and objects, ultimately enhancing the fidelity and practicality of computer graphics applications in various domains.

In this paper, we introduce a particle-based SPH framework for simulating hyperelastic materials with anisotropic stiffness models. As is shown in Fig. 1, we couple an implicit divergence-free SPH solver with particle-based deformation gradient computation and apply various elastic energy functions to achieve incompressible elastic simulations. The incompressibility of elastic objects and collisions between different bodies are also managed by the implicit SPH algorithm [11]. To incorporate anisotropic properties, we integrate anisotropic energy functions constructed from the extrapolation of Cauchy–Green invariants [12]. By integrating activation and contraction coefficients into the energy functions, particles can simulate muscle contractions and lift heavy objects. Our method effectively represents elastic objects with varying mechanical properties across different directions and can be further employed to mimic muscle contractions.

In conclusion, this work presents a novel approach to simulating hyperelastic materials with anisotropic stiffness models using a particle-based SPH framework. Our method addresses the current gap in anisotropic elastic simulation studies for particle-based techniques and offers a more robust and versatile solution compared to traditional mesh-based methods. Positioned within the broader research landscape, this work contributes to the ongoing development of more accurate, efficient, and adaptable simulation methods for hyperelastic materials. Through a series of experiments, we demonstrate that our approach can provide realistic simulations for a wide range of animal and human body movements, underscoring its potential for diverse applications in computer graphics, biomechanics, and material science.

2. Related work

The simulation of deformable objects with physics-based models has a long history in computer graphics. A vast range of methods have been proposed to achieve a detailed and realistic effect of deformable objects. The early research on deformable objects is introduced in Nealen [13] work.

Particle-based methods. Among these typical methods, the mass–spring system is a simple and early particle-based approach to implement for simulating deformable materials. As a result, mass–spring systems are widely used for a range of deformable objects, like cloth [14], geometrically complex deformable solids [15] and hair [16]. Liu et al. [17] subsequently proposed a new implicit Euler numerical method for dynamics of mass–spring systems, which has been applied to simulate the motion of cloth pieces, wiring harnesses, bulk objects, and character clothing.

Though the above mentioned methods are easy to implement, explaining the physics-based simulation of deformable bodies remains a significant challenge. The deformation gradient in physics formulation is difficult to incorporate into the mass–spring systems, while some other particle-based methods could resolve these problems. One of the most compelling approaches is the SPH methods which are well known for their behavior of simulating fluid [18,19] and fluid–rigid interaction [20]. Its Lagrangian property allows the displacement field and gradient deformation to be easily evaluated by exploiting the gradient of the smoothing kernel, which is quite attractive to the simulation of deformable objects. Desbrun and Gascuel [21] first introduced the SPH methods into the simulation of inelastic deformable objects and viscous fluids. However, a key problem is that the standard SPH kernel gradient evaluation is not first-order consistent, which means that the rotation of the deformation cannot be captured. Müller et al. [22] proposed a particle-based approach to simulate a wide range of elastically and plastically deformable objects which can melt, flow, solidify split and merge. They used the Moving Least Squares (MLS) procedure to compute the spatial derivatives of the discrete displacement field to obtain strain and stress. Becker et al. [8] introduced a novel corotated SPH formulation for deformable elastic solids that solves the missing rotational invariance of previous approaches and is capable of calculating elastic forces for a wide range of scenes using the linear Cauchy–Green tensor. However, their method only considers the elastic deformation, Zhou et al. [23] presented a novel particle-based method for simulating elastoplastic materials with implicit numerical integration on a sparse linear system, allowing for a wider range of stiffness and plasticity settings.

In recent years, several studies have explored SPH methods for simulating elastic objects due to their ability to provide a unified framework for simulating different materials, such as rigid bodies and fluid mixtures. Peer et al. [5] focused on the rotation of the linear infinitesimal strain tensor. They used a correction matrix to ensure the first-order consistency of the kernel gradient and capture a rotation extraction directly from the SPH deformation gradient. They proposed implicit formulation and adapted rotation estimation that enables significantly larger time steps and higher stiffness for the simulation of deformable objects. Building on this work, Gissler et al. [24] fixed the wrong velocity of the elastic objects during the iteration in Akinci [20] approach, and corrected the pressure between fluid and solid. They introduced Peer [5] method to realize the bidirectional coupling between fluid and deformable solid. Gissler et al. [25] subsequently proposed an elastoplastic SPH approach for snow that combines two implicit solvers guided by Peer [5] work and simulated various snow effects such as snow fall and accumulation, deformation, breaking, compression and hardening. Kugelstadt et al. [26] introduced a SPH operator splitting formulation of the corotated linear elastic material model, which enables faster time-stepping than the state-of-the-art method by Peer [5].

FEM/Mesh methods. In addition to the aforementioned particle-based methods, the FEM is another attractive approach for simulating elastic objects, as it can compute an explicit deformation function and enable the reversal of deformations with precision. The theory of FEM simulation of deformable solids has been introduced in Sifakis [4] work. However, the deformation function becomes ill-conditioned when there is a significant plastic flow (permanent deformation), leading to numerical instability in the simulation. Bargteil et al. [27] presented extensions to standard finite element methods that allow for simulating large plastic flow in solid materials. Kharevych et al. [28] used homogenization theory to allow for the approximation of a deformable object made of arbitrary fine structures of various linear elastic materials with a dynamically similar coarse model. To simulate volumetric deformable bodies with nonlinear rest shape, Bargteil et al. [29] developed a quadratic tetrahedral element based on the Bézier basis for graphical animation of deformable bodies. In [30], Xu et al. presented a new method with the gradient of SVD for simulating nonlinear materials using the principal stretches of the material and applied this method to isotropic and anisotropic material design for soft-body simulation in computer animation. Afterwards, Smith et al. [31] extended a novel Neo-Hookean elasticity model that maintains the fleshy appearance of the Neo-Hookean model and exhibits superior volume preservation. Kugelstadt et al. [32] presented a method based on a volumetric approach using tetrahedral elements to represent the shape of the object, which allows for more accurate and realistic simulation and simulated the complex deformation of soft objects without introducing numerical artifacts in real-time using corotated finite elements. Smith et al. [33] resolved Hessian indefiniteness by investigating eigenstructures analytically and presented closed-form expressions for the eigenvalues and eigenvectors of all tensor invariant. Kim et al. [34] used the FEM with a new formulation of the Baraff-Witkin cloth model. This model is shown to be a coupled anisotropic strain energy, with a stretching term that approximates the isotropic As-Rigid-As-Possible (ARAP) energy. Kim et al. [9] proposed a robust, inversion-safe anisotropic model called the Anisotropic ARAP energy. They presented a rehabilitation approach that allows badly-conditioned elements to be simulated robustly and efficiently. They used FEM methods to implement the behavior of anisotropic hyperelasticity, specifically transverse isotropy.

MPM methods. In recent years, the Material Point Method (MPM) has become a popular approach for multi-material simulation due to its advantages over both particles and meshes. Stomakhin et al. [35] first introduced this method to simulate snow and phase changes of snow as elastoplastic materials. Afterwards, Jiang et al. [36] resolved the large dissipation or instabilities during the transfer between the particles and meshes by augmenting each particle with a locally affine description of the velocity. In [37], Hu et al. extended their ideas and used MLS to replace the shape functions in the stress divergence term. This enables the simulation of various richer phenomena and results in a double speed up and easier implementation. Daviet and Bertails-Descoubes [38] developed a model for granular materials that behave like solids due to internal friction. They represented granular matter as a compressible viscoplastic fluid combined with a Drucker–Prager yield criterion and a unilateral compressibility constraint. In [39], Jiang et al. designed anisotropic hyperelastic constitutive models to characterize the response of manifold strain and shear. They also proposed an elastoplastic constitutive model defining the collision response, which can process collision-intensive scenes with millions of degrees of freedom in just a few minutes per frame. In [40], Schreck and Wojtan built a generalized model of anisotropy that can be integrated into current MPM elastoplasticity solvers and an orthotropic law reducing the complexity of the generalized model, which provides a more efficient and effective simulation of anisotropic materials.

In conclusion, the above methods have provided comprehensive insight into isotropic elastoplastic solids. However, for anisotropic elastic objects, recent relevant research has primarily adopted meshed-based FEM and MPM methods. This paper introduces the particle-based method to simulate anisotropic elastic materials, combining the SPH method framework with the anisotropic energy function to achieve the simulation of hyperelastic materials with anisotropic stiffness models.

3. Deformation gradient in SPH and energy functions

3.1. Computation of physical values using SPH approach

In the SPH method, the continuum is discretized into a set of particles, each representing a volume element of the fluid. The physical properties of the fluid, such as density, pressure, and velocity, are then calculated by approximating the values at each particle based on the values of neighboring particles.

One of the key equations used in SPH is the approximation of a physical quantity A at a particle i, which can be expressed as:

$$A(\mathbf{x}_i) = \sum_j A(\mathbf{x}_j) V_j W(\mathbf{x}_i - \mathbf{x}_j, h), \tag{1}$$

where $\mathbf{x}_i$ and $\mathbf{x}_j$ are the positions of particles i and j, respectively, V_j is the volume associated with particle j, h is the smoothing length used to define the influence radius of a particle, and W is the smoothing kernel function that assigns weights to neighboring particles based on their distance from the current particle. Eq. (1) essentially states that the value of A at particle i is a sum of the values of A at all neighboring particles j, weighted by their volumes and the smoothing kernel function. This approach allows for a continuous approximation of physical properties across the fluid, and has been shown to be effective in simulating a wide range of fluid phenomena.

To extrapolate this idea, the gradient of A can be computed using the same approach as Eq. (1). The gradient of A at a particle i can be approximated as:

$$\nabla A_i = \sum_j A_j V_j \nabla_i W_{ij}, \tag{2}$$

where A_i, A_j is the abbreviation of $A(\mathbf{x}_i)$ and $A(\mathbf{x}_j)$. $\nabla_i W$ is the gradient of the smoothing kernel function with respect to the position of particle i. And W_{ij} is the short form of $W(\mathbf{x}_i - \mathbf{x}_j, h)$. To further reduce the higher order error, we can use the property of $\nabla 1 = \mathbf{0}$ and modify Eq. (2) to $\nabla A(\mathbf{x}_i) - A(\mathbf{x}_i)\nabla 1$ to get:

$$\nabla A_i = \sum_j A_{ji} V_j \nabla_i W_{ij}, \tag{3}$$

where A_{ji} represents $A_j - A_i$. In the following we will use Eq. (3) for all SPH gradient-related computation.

3.2. Deformation gradient

The deformation gradient is a tensor that characterizes the deformation of a material. In the context of continuum mechanics, it serves as a mean to relate the deformed state of a material to its undeformed state. Mathematically, the deformation gradient, denoted as $\mathbf{F}$, is a second-order tensor defined as:

$$\mathbf{F} = \frac{\partial \mathbf{x}}{\partial \bar{\mathbf{x}}}, \tag{4}$$

where $\mathbf{x}$ represents the current position of a particle in the deformed state, and $\bar{\mathbf{x}}$ corresponds to its initial position in the undeformed state. The deformation gradient $\mathbf{F}$ encapsulates the local stretching, compression, and rotation of the material at each point within the domain.

In order to compute the deformation gradient using the SPH method, we can employ an approach analogous to Eq. (3). In this case, the physical value A corresponds to the particles' positions in the deformed state, while the relative positions between them are equivalent to the initial positions. Consequently, we arrive at:

$$\mathbf{F}_i = \sum_j \mathbf{x}_{ji} V_j \otimes \nabla_i W_{\bar{ij}}, \tag{5}$$

where $\otimes$ denotes the outer product, and $\nabla_i W_{\bar{ij}}$ represents $W(\bar{\mathbf{x}}_i - \bar{\mathbf{x}}_j, h)$. However, similar to the preference for using Eq. (3) over Eq. (2) for computing gradients, computational errors may arise when directly applying Eq. (5) to calculate the deformation gradient near object boundaries. Owing to the absence of neighboring particles, the condition $\mathbf{F}(\bar{\mathbf{x}}_i) = \sum_j (\bar{\mathbf{x}}_j - \bar{\mathbf{x}}_i) V_j \otimes \nabla_i W_{\bar{ij}} = \mathbf{I}$, with $\mathbf{I}$ as the identity matrix, may not hold for undeformed positions. To rectify this error, we can add $\mathbf{F}^{-1}(\bar{\mathbf{x}}_i)$ to $\nabla_i W_{\bar{ij}}$ in Eq. (5) as a weight matrix.

The deformation gradient tensor, $\mathbf{F}$, can be utilized to compute the strain tensor, which quantifies the extent to which a material has been deformed. Subsequently, the strain tensor can be employed to calculate stress, which measures the forces exerted on the material.

3.3. Energy functions

In the study of hyperelastic materials, energy functions play a crucial role in relating the deformation of a material to the forces acting upon it. An energy function, typically denoted as Ψ, represents the strain energy density of a material. It is a scalar function that quantifies the amount of energy stored in a material as a result of its deformation. This stored energy arises due to the internal resistance of the material to deformation and is dissipated when the material returns to its undeformed state.

The purpose of the energy function is to describe the material's mechanical behavior under various deformation states. The energy function depends on the deformation gradient $\mathbf{F}$ and can be used to derive the first Piola–Kirchhoff stress tensor (PK1) $\mathbf{P}$, which is related to the forces exerted on a material. The relationship between the energy function Ψ and the stress tensor $\mathbf{P}$ is given by:

$$\mathbf{P}(\mathbf{F}) = \frac{\partial \Psi}{\partial \mathbf{F}}, \tag{6}$$

Different energy functions can be designed and employed to model various material behaviors. For hyperelastic materials, the key factors for designing a successful energy function are to ensure the function can accurately capture the local material's stretches and compressions while remaining unaffected by its rotation and translation. Some of the classical energy functions and their first Piola–Kirchhoff stress tensors are listed in Table 1. In these expressions, μ and λ represent Lamé's first and second parameters, respectively. The further related tensors used in these energy functions are shown in Table 2.

Table 1
Energy functions.

Linear elasticity	$\Psi_{\mathrm{LE}} = \mu \,\|\|\boldsymbol{\epsilon}_l\|\|_F^2 + \frac{\lambda}{2}\,\mathrm{tr}^2(\boldsymbol{\epsilon}_l)$ $\mathbf{P}_{\mathrm{LE}}(\mathbf{F}) = 2\mu\boldsymbol{\epsilon}_l + \lambda\,\mathrm{tr}(\boldsymbol{\epsilon}_l)\,\mathbf{I}$
Co-rotated linear elasticity	$\Psi_{\mathrm{CR}} = \mu \,\|\|\boldsymbol{\epsilon}_c\|\|_F^2 + \frac{\lambda}{2}\,\mathrm{tr}^2(\boldsymbol{\epsilon}_c)$ $\mathbf{P}_{\mathrm{CR}}(\mathbf{F}) = \mathbf{R}\,[2\mu\boldsymbol{\epsilon}_c + \lambda\,\mathrm{tr}(\boldsymbol{\epsilon}_c)\,\mathbf{I}]$
St. Venant-Kirchhoff elasticity	$\Psi_{\mathrm{StVK}} = \mu \,\left\|\left\|\boldsymbol{\epsilon}_g\right\|\right\|_F^2 + \frac{\lambda}{2}\,\mathrm{tr}^2(\boldsymbol{\epsilon}_g)$ $\mathbf{P}_{\mathrm{StVK}}(\mathbf{F}) = \mathbf{F}\left[2\mu\boldsymbol{\epsilon}_g + \lambda\,\mathrm{tr}(\boldsymbol{\epsilon}_g)\,\mathbf{I}\right]$
As-Rigid-As-Possible elasticity	$\Psi_{\mathrm{ARAP}} = \frac{\mu}{2}\,\|\|\boldsymbol{\epsilon}_c\|\|_F^2$ $\mathbf{P}_{\mathrm{ARAP}}(\mathbf{F}) = \mu\mathbf{R}\boldsymbol{\epsilon}_c$
Neo-Hookean elasticity	$\Psi_{\mathrm{Neo}} = \frac{\mu}{2}\left(\|\|\mathbf{F}\|\|_F^2 - 3\right) - \mu\log(J) + \frac{\lambda}{2}\log^2(J)$ $\mathbf{P}_{\mathrm{Neo}}(\mathbf{F}) = \mu\left(\mathbf{F} - \mathbf{F}^{-T}\right) + \lambda\log(J)\,\mathbf{F}^{-T}$

Table 2
Tensor notations.

Infinitesimal strain	$\boldsymbol{\epsilon}_l = \frac{1}{2}\left(\mathbf{F} + \mathbf{F}^T\right) - \mathbf{I}$
Co-rotated strain	$\boldsymbol{\epsilon}_c = \mathbf{S} - \mathbf{I}$
Green strain	$\boldsymbol{\epsilon}_g = \frac{1}{2}(\mathbf{C} - \mathbf{I})$

The comparison of the forms of Linear elasticity, Co-rotated linear elasticity, and St. Venant-Kirchhoff elasticity depicted in these tables reveals their similarities, the only distinct factor being the strain tensors inherent to each. The As-Rigid-As-Possible elasticity model can be construed as the initial term in the co-rotated energy equation. As referenced in Table 2, the Cauchy–Green Tensor is denoted as $\mathbf{C} = \mathbf{F}^T\mathbf{F}$, while $\mathbf{S}$ symbolizes the stretching component of $\mathbf{F}$ following the polar decomposition $\mathbf{F} = \mathbf{R}\mathbf{S}$. Both $\boldsymbol{\epsilon}_g$ and $\boldsymbol{\epsilon}_c$ are impervious to the rotational component in $\mathbf{F}$. The removal of the $\mathbf{R}$ part visibly substantiates this immunity for $\boldsymbol{\epsilon}_c$. For $\boldsymbol{\epsilon}_g$, we can perform singular value decomposition (SVD) on $\mathbf{F}$ and find that $\mathbf{F}^T\mathbf{F} = \mathbf{V}\boldsymbol{\Sigma}^T\mathbf{U}^T\mathbf{U}\boldsymbol{\Sigma}\mathbf{V}^T = \mathbf{V}\boldsymbol{\Sigma}^2\mathbf{V}^T$ contains only the square of the stretching. However, for Linear elasticity using the Infinitesimal strain, the rotation part cannot be efficiently eliminated during the computation. Special care must be taken in Eq. (5) to produce a rotation-aware deformation gradient computation.

The Neo-Hookean elasticity model stands out from the other four models due to its ability to preserve the size of objects in both linear and volumetric scales. This unique characteristic can be observed by examining the Cauchy–Green invariants in Table 3, where I_1, I_2, and I_3 are invariants that describe the deformation of an elastic element over time. In the table, σ denotes the singular values found in the matrix $\boldsymbol{\Sigma}$, which results from the polar decomposition of $\mathbf{F}$, while j signifies the number of dimensions. I_1 and I_2 represent the quadratic and quartic combinations of all singular values, respectively. Both of these invariants return to 2 or 3 when an elastic object is neither compressed nor expanded in 2D or 3D space. Conversely, I_3 calculates the product of all singular values, representing the area or volume of the elastic element.

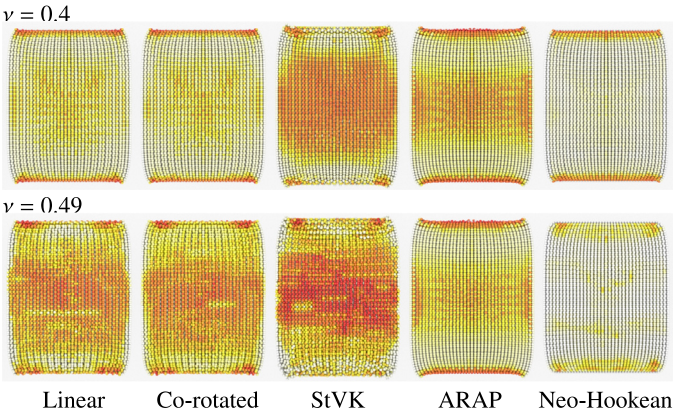

Fig. 2. Elastic cuboid squashing experiments employing five different energy functions, with Young's modulus of $E = 5 \times 10^4$ Pa for all cases. The figure uses color-coding to represent the forces applied to the particles, with more intense colors indicating a higher degree of resistance.

Table 3
The Cauchy–Green invariants (row 1–3) and their anisotropic extended forms (row 4–5).

I_1	$\mathrm{tr}(\mathbf{C}) = \sum_j \sigma_j^2$
I_2	$\mathrm{tr}(\mathbf{C}^2) = \sum_j \sigma_j^4$
I_3	$\det(\mathbf{C}) = \det(\mathbf{F}^T\mathbf{F}) = \prod_j \sigma_j^2$
I_4^{ext}	$\mathbf{a}^T\mathbf{S}\mathbf{a} = \sum_j \tilde{a}_j^2 \sigma_j$
I_5^{ext}	$\mathbf{a}^T\mathbf{F}^T\mathbf{F}\mathbf{a} = \sum_j \tilde{a}_j^2 \sigma_j^2$

By converting the energy functions in Table 1 into the form of Cauchy–Green invariants, we get

$$\begin{aligned}
\Psi_{\mathrm{LE}} &= \mu\,(I_1 - 2\,\mathrm{tr}(\mathbf{F}) + 3) + \frac{\lambda}{2}\,(\mathrm{tr}(\mathbf{F}) - 3)^2 \\
\Psi_{\mathrm{CR}} &= \mu\,(I_1 - 2\,\mathrm{tr}(\mathbf{S}) + 3) + \frac{\lambda}{2}\,(\mathrm{tr}(\mathbf{S}) - 3)^2 \\
\Psi_{\mathrm{StVK}} &= \frac{\mu}{4}\,(I_2 - 2I_1 + 3) + \frac{\lambda}{8}\,(I_1 - 3)^2 \\
\Psi_{\mathrm{ARAP}} &= \frac{\mu}{2}\,(I_1 - 2\,\mathrm{tr}(\mathbf{S}) + 3) \\
\Psi_{\mathrm{Neo}} &= \frac{\mu}{2}\,(I_1 - 3) - \mu \log\left(\sqrt{I_3}\right) + \frac{\lambda}{2}\left(\log\sqrt{I_3}\right)^2
\end{aligned} \tag{7}$$

under 3-dimensional space condition and we can see that not only Ψ_{LE} is not rotation-free, but also only Ψ_{Neo} contains I_3 to conserve the total volume.

Figs. 2 and 3 illustrate two sets of experiments designed to assess the efficacy of various energy functions in squash and stretch scenarios. The linear energy model employed was modified using the procedure outlined in [5] to eliminate rotation from the deformation gradient. An elastic cuboid was subjected to these squash and stretch manipulations, with a color gradient from white to red indicative of the resistance force magnitude at each particle.

Despite differences in force distribution across the five energy models, they all exhibit analogous deformations with a Poisson's ratio of $\nu = 0.4$. Notably, the linear energy and co-rotated energy models display nearly identical force distributions, resulting from the preservation of a similar set of Cauchy–Green invariants.

An intriguing scenario arises when the cuboid is stretched under the ARAP energy: there is no observed horizontal shrinkage concurrent with vertical stretching. This outcome arises from the shear modulus λ being zero in the ARAP energy function (refer to Table 1), which leads to a zero Poisson's ratio. Hence, dimensional stretching and compression do not interfere with each other. The observed bulging in the compression experiment is attributable to the utilization of incompressible SPH solvers.

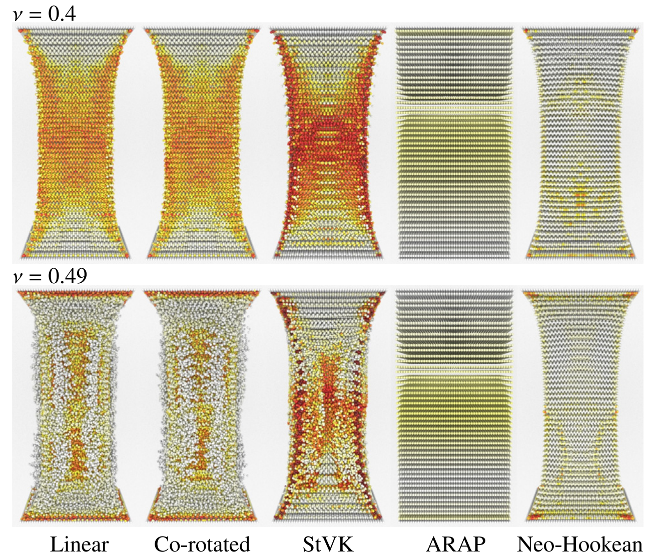

Fig. 3. Elastic cuboid stretching experiments employ five different energy functions, with Young's modulus of $E = 5 \times 10^4$ Pa for all cases. The figure uses color-coding to represent the forces applied on the particles, with more intense colors indicating a higher degree of resistance.

When the Poisson's ratio is increased to $\nu = 0.49$ to simulate a near-incompressible state, significant instability is noticed in both the linear and co-rotated energy functions. Further, perceptible jitters surface in the StVK model during the stretching experiment, while the Neo-Hookean model maintains stability. This instability can be traced to the lack of the I_3 term in the first three models, thus impeding their ability to effectively preserve volumes.

4. Anisotropic energy function

4.1. Anisotropic invariants

To incorporate anisotropic stiffness into an object, we need to combine additional anisotropic energy with the traditional isotropic energy. First, we determine a direction for the anisotropic constraint, represented as a unit vector **a**. Then, we ensure that the anisotropic energy responds only to deformations along **a** and remains unaffected by deformations perpendicular to it. We achieve this by projecting the singular values of all dimensions onto the **a** direction.

We follow the ideas from previous papers [10] and describe the stretching state of the elastic element with the matrix **S**, obtained from the deformation gradient without rotation. The SVD of this rotation-free matrix is given by $\mathbf{S} = \mathbf{V}\boldsymbol{\Sigma}\mathbf{V}^T$. To incorporate the direction vector **a** into $\boldsymbol{\Sigma}$, we rotate **a** into the stretching space by multiplying it with $\mathbf{V}^T$, resulting in $\tilde{\mathbf{a}} = \mathbf{V}^T\mathbf{a}$. The probed singular values then take the form:

$$\tilde{\boldsymbol{\Sigma}} = \boldsymbol{\Sigma}\mathbf{V}^T\mathbf{a}. \tag{8}$$

To construct energy functions, we can apply the anisotropically filtered singular values. However, to avoid the actual need for computing SVD, I_5^{ext} is employed in [10]. In I_5^{ext}, the rotation part is canceled out, similar to I_1. In [12], Kim and Eberle further pointed out that the sum of the weighted squares of eigenvalues fails to capture negativity, resulting in an inability to effectively

Algorithm 1 Anisotropic smoothed particle hydrodynamics solver

1: **for** all particles i **do**
2: search all neighbor particles j
3: **end for**
4: **while** simulation is running **do**
5: **procedure** ADVECTION STEP
6: **for** all particles i **do**
7: deformation gradient $\mathbf{F}_i$ (Eqn. (4))
8: isotropic energy function $\Psi_{iso,i}$ (Tab. 1)
9: isotropic PK1 tensor $\mathbf{P}_{iso,i}$ (Tab. 1)
10: anisotropic energy and its according PK1 $\mathbf{P}_{ani,i}$ (Eqn. (9) , (12))
11: elastic force $\mathbf{f}_i^{ela}$ (Eqn. (17))
12: add gravity as advection force $\mathbf{f}_i^{adv} = \mathbf{f}_i^{ela} + \mathbf{f}_i^{gra}$
13: update advection velocity $\mathbf{v}_i^{adv} = \mathbf{v}_i(t) + \mathbf{f}_i^{adv}\Delta t$
14: **end for**
15: **end procedure**
16: **procedure** INCOMPRESSIBLE SOLVER
17: **while** $\mathbf{v}_i^{adv}$ is compressible **do**
18: **for** all particles i **do**
19: update advection velocity $\mathbf{v}_i^{adv}$ =imcomp-solver($\mathbf{v}_i^{adv}$)
20: **end for**
21: **end while**
22: **for** all particles i **do**
23: update velocity and position $\mathbf{v}_i = \mathbf{v}_i^{adv}$, $\mathbf{x}_i = \mathbf{x}_i(t) + \mathbf{v}_i\Delta t$
24: **end for**
25: **end procedure**
26: **procedure** DIVERGENCE-FREE SOLVER
27: **while** $\mathbf{v}_i$ is not divergence-free **do**
28: update velocity field $\mathbf{v}_i$ =div-free-solver($\mathbf{v}_i$)
29: **end while**
30: **end procedure**
31: **end while**

capture the inversion of elements. To address this issue, they proposed sign-preserving invariant I_4^{ext} as a substitute.

4.2. Anisotropic functions

An anisotropic energy function is ideally formulated to solely influence the elastic force in direction $\mathbf{a}$, while remaining unaffected by the other two orthogonal directions in a 3-dimensional space. As per the experiments conducted in Figs. 2 and 3, the Isotropic ARAP model recommends maintaining $\lambda = 0$ when devising the anisotropic model. In this study, we adopt the inversion-safe variant of the anisotropic energy function proposed in [9], expressed as:

$$\Psi_{ani} = \frac{\mu}{2}\left(\sqrt{I_5^{ext}} + \operatorname{sgn}(I_4^{ext})\right)^2, \tag{9}$$

$$\mathbf{P}_{ani} = \mu\left(1 - \frac{\operatorname{sgn}(I_4^{ext})}{\sqrt{I_5^{ext}}}\right)\mathbf{FA}, \tag{10}$$

where sgn denotes the signum function as:

$$\operatorname{sgn}(x) = \begin{cases} -1 & \text{if } x < 0 \\ 0 & \text{if } x = 0 \\ 1 & \text{if } x > 0. \end{cases} \tag{11}$$

The signum function in Eq. (9) ensures that the value of Ψ_{ani} reaches its minimum at the undeformed state and gradually increases for both compression and stretching. This formulation successfully avoids the bimodal minimum issue that occurs in previous anisotropic methods, where another minimum appears in the negative singular value state.

To model muscle contraction and relaxation, we introduce two additional variables into Eq. (9) to flexibly adjust the effect of anisotropic energy:

$$\Psi_{ani}^{mus} = c_a\left(\sqrt{I_5^{ext}} + c_l \operatorname{sgn}(I_4^{ext})\right)^2, \tag{12}$$

$$\mathbf{P}_{ani}^{mus} = 2c_a\left(1 - c_l\frac{\operatorname{sgn}(I_4^{ext})}{\sqrt{I_5^{ext}}}\right)\mathbf{FA}, \tag{13}$$

where c_a is the activation coefficient, which describes the force of contraction, and c_l is the length coefficient, which determines how much the muscle should shrink. As can be seen from Eq. (9), the graph of this energy function is a quadratic curve. The coefficient c_a controls the steepness of the curve, while c_l determines the value of I_4^{ext} at which the curve reaches its minimum point.

5. Force computation

5.1. Elastic force

After obtaining both isotropic and anisotropic energies Ψ_{iso} and Ψ_{ani}, as well as the resulting PK1 stress tensors $\mathbf{P}_{iso}$ and $\mathbf{P}_{ani}$, we can compute the final stress tensor as:

$$\mathbf{P}_{fin} = \mathbf{P}_{iso} + \mathbf{P}_{ani}. \tag{14}$$

To ultimately derive the force from the stress tensor as $\mathbf{f} = V\nabla\cdot\mathbf{P}$, while preserving the conservation of momentum between particles, we utilize the SPH computation form in [8] to ensure that the elastic forces between two particles are equivalent. The elastic force from particle j to the neighboring particle i, according to Eq. (2), is:

$$\mathbf{f}_{j\to i}^{ela} = V_i V_j \mathbf{P}_i \nabla_i W_{\tilde{i}\tilde{j}}. \tag{15}$$

We should also note that particle i exerts forces on j as:

$$\mathbf{f}_{i\to j}^{ela} = V_i V_j \mathbf{P}_j \nabla_j W_{\tilde{j}\tilde{i}}. \tag{16}$$

To conserve the momentum for the entire system, the elastic force experienced by i takes the following form:

$$\begin{aligned}\mathbf{f}_i^{ela} &= \sum_j \mathbf{f}_{j\to i}^{ela} - \sum_j \mathbf{f}_{i\to j}^{ela} \\ &= \sum_j V_i V_j\left(\mathbf{P}_i\nabla_i W_{\tilde{i}\tilde{j}} - \mathbf{P}_j\nabla_j W_{\tilde{j}\tilde{i}}\right).\end{aligned} \tag{17}$$

5.2. Divergence-free incompressibility

In order to apply the strong incompressibility into the elastic object, we incorporate the elastic simulation with divergence-free constraint from [19]. The elastic force acts as a part of the advection procedure during the whole advection-projection scheme. As is shown in Algorithm 1, the elastic force computation corresponds to the line 7–11 of the advection step procedure. Then combined with the force from gravity (if needed), we can get the advection velocity in line 13.

Two iterative solvers from [19] take place after the advection step. The first incompressible solver from line 16–25 updates both velocity and position for each particle to arrive at incompressible state at the next time step. The divergence-free solver (line 26–30) then further adjust the velocity field at the next time step to a divergence-free state to ensure a more robust simulation condition.

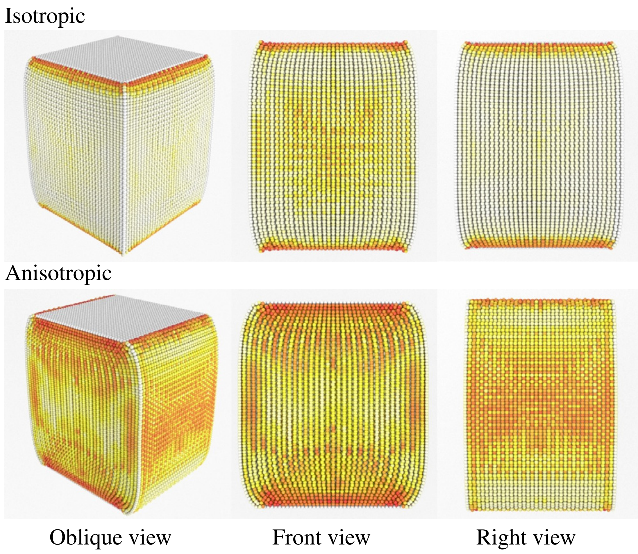

Fig. 4. Elastic cuboid squashing experiments utilizing both isotropic and a combination of isotropic and anisotropic energies, with Young's modulus of $E = 5 \times 10^4$ Pa for all cases. The figure employs color-coding to represent the forces applied on the particles, with more intense colors indicating a higher degree of resistance. The Neo-Hookean energy is used.

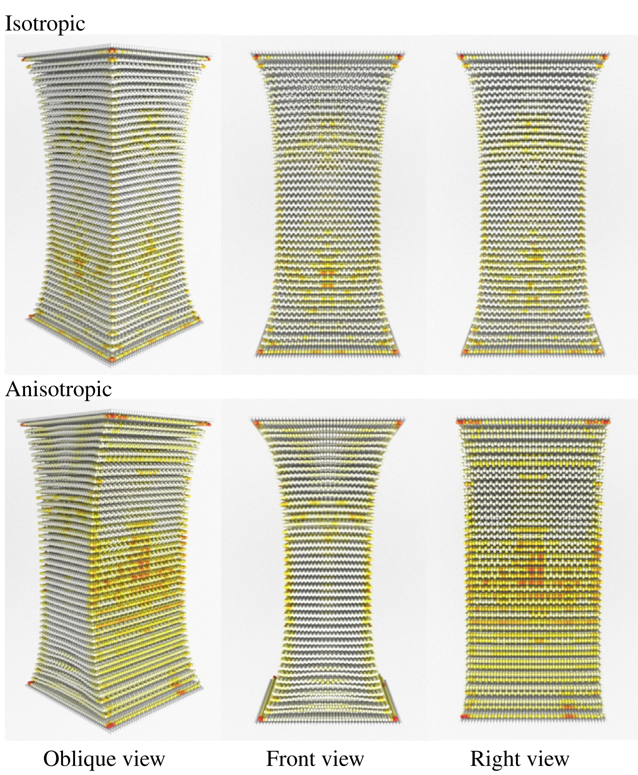

Fig. 5. Elastic cuboid stretching experiments utilizing both isotropic and a combination of isotropic and anisotropic energies, with Young's modulus of $E = 5 \times 10^4$ Pa for all cases. The figure employs color-coding to represent the forces applied on the particles, with more intense colors indicating a higher degree of resistance. The Neo-Hookean energy is used.

6. Experiments

This section delineates multiple sets of experiments designed to validate the effectiveness and capabilities of the proposed anisotropic model, which relies on particle-based methodology.

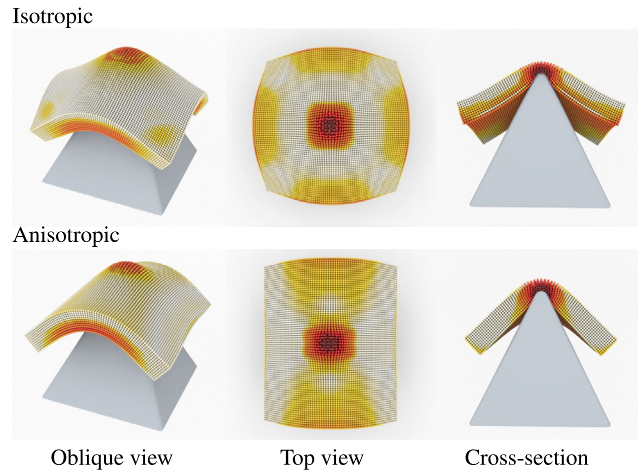

Fig. 6. An elastic pad falls onto a tetrahedral pyramid. The figure employs color-coding to represent the forces applied on the particles. In the first row of isotropic elasticity experiments, the pad is subjected to uniform force in the horizontal direction. In the second row of anisotropic experiments, the force on the pad exhibits directionality, causing significant bending in only one direction. The anisotropy direction is along the y axis of the top view.

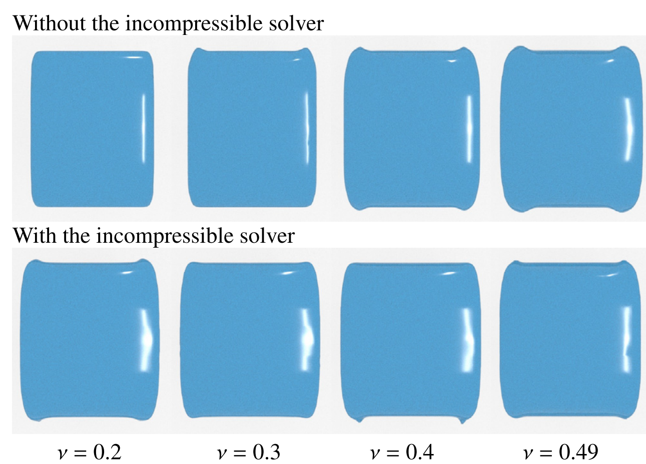

Fig. 7. Elastic cuboid squashing experiments with Young's modulus of $E = 5 \times 10^4$ Pa for all cases, conducted under various Poisson's ratios. In the first row, all experiments are simulated without the divergence-free SPH constraint. In the second row, the SPH constraint is applied to all cases.

Several experiments are color-coded (Figs. 2, 3, 4, 5, 6) to intuitively illustrate the magnitude of the elastic force exerted on particles, with deeper hues indicating stronger forces. We adopt the elastic coupling method from [11] for handling object coupling.

6.1. Anisotropic elasticity

Anisotropic cuboid squashing and stretching. In the experiments shown in Figs. 2, 3, we assessed the anisotropic elasticity energy based on the Neo-Hookean model, where the anisotropy direction was set as $\mathbf{a} = [1, 0, 0]^T$. Observations from three distinctive viewpoints confirm that elastomers display increased stiffness along the anisotropy direction. Figs. 4 and 5 reveal that under isotropic elasticity, the material uniformly compresses in all dimensions, while anisotropic elasticity results in more pronounced expansion in the direction orthogonal to the anisotropy direction.

Cone impact. To contrast the responses of anisotropic and isotropic materials to sudden impacts, we executed an experiment

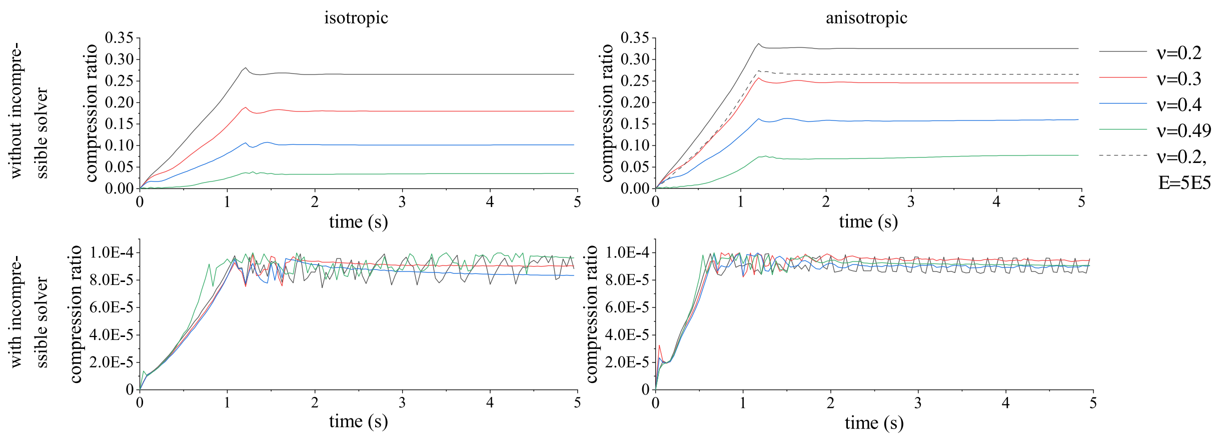

Fig. 8. Comparison of compressibility with or without the SPH incompressible solver in elasticity compression experiments in Fig. 7. The four panels represent various conditions: isotropic elasticity without the incompressible solver (top left), anisotropic elasticity without the incompressible solver (top right), isotropic elasticity with the incompressible solver (bottom left), and anisotropic elasticity with the incompressible solver (bottom right). In all experiments, the Young's modulus is set to $E = 5 \times 10^4$ Pa, except in one instance where $E = 5 \times 10^5$ Pa, as indicated in the top right panel.

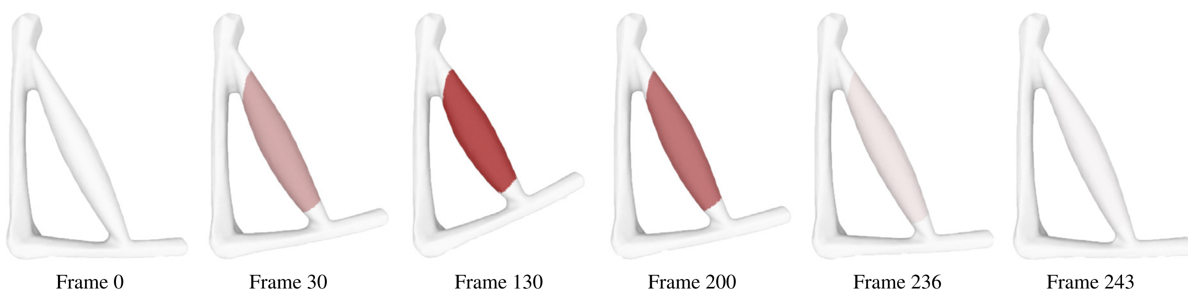

Fig. 9. Muscle contraction and relaxation drive bone movement. The activation length is set to $c_l = 0.4$ in this experiment. The red color indicates the level of muscle activation, with white representing no activation.

involving the fall of an elastic object onto a pyramid under both conditions. In the overhead view, upper particles were removed to facilitate observation of the elastic forces impacting the internal particles. As seen in Fig. 6, under isotropic conditions, the internal forces within the elastic object are homogeneously distributed, while more intense colors underscore an increased elastic force in the anisotropic direction.

6.2. Incompressibility from implicit SPH

Cuboid compression: with and without implicit SPH incompressibility. We investigated the compression effect with and without the incompressible solver, modulating Poisson's ratio between 0.2 and 0.49. Fig. 7 shows that absent an incompressible solver, Poisson's ratio directly influences the degree of compression, with larger ratios leading to reduced elastic compressibility and enhanced extrusion. When an implicit incompressibility constraint is integrated into the simulation, even a significantly lower Poisson's ratio (< 0.5) can yield a stable incompressible state.

Numerical analysis. We further evaluated the overall compression ratio for this experiment in Fig. 8. The simulation results indicate that while Poisson's ratio remains constant, altering Young's modulus does not affect compressibility when the incompressible constraint is applied, as evidenced on the right of Fig. 8. The compression ratio deviates within a minimal range. Intriguingly, as the black line grouping shows, maintaining the Young's modulus constant while varying Poisson's ratio does not modify the compressible state. However, adding further anisotropic constraints may increase the compressibility of the elastic object, thereby underlining the crucial role of incompressibility maintenance for elastic components.

6.3. Muscle simulation

Exploring the utility of our approach for animation and special effects, we simulated the distinct movements of a human bicep and a crawling snake.

Bicep contraction. We modeled the influence of muscle contraction and relaxation on bone motion (Fig. 9). By progressively increasing the activation factor (indicated by color intensity), we induced muscle contraction, leading to bone elevation. Subsequent reduction in the activation coefficient prompted muscle relaxation and extension of the bone, demonstrating our method's aptitude for realistic muscle motion simulation.

Crawling snake. In a separate experiment, we precisely modeled a snake's crawling motion by manipulating the contraction and expansion of two muscles in its head (Figs. 10, 11). This induced a twisting motion in the snake's body, propelling forward movement. The cyclical muscle control faithfully emulated real snake locomotion, providing a convincing portrayal of the situation.

6.4. Advanced eye movement modeling

Historically, the simulation of eye movement in computer graphics has posed substantial challenges. Typically, prior models relied heavily on geometric transformations and animations to represent complex and nuanced ocular motions. However, these methods often fell short of accurately capturing the sophisticated interplay between the eyeball and its surrounding musculature.

Building on this traditional framework, we refined our approach to eye movement simulation by employing the anisotropic

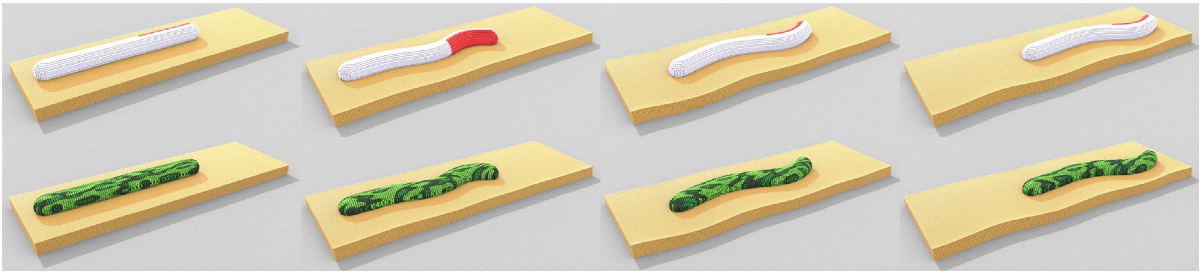

Fig. 10. Simulating snake crawling by controlling the contraction of left and right head muscles. The red particles represent activated and shrinking muscle segments.

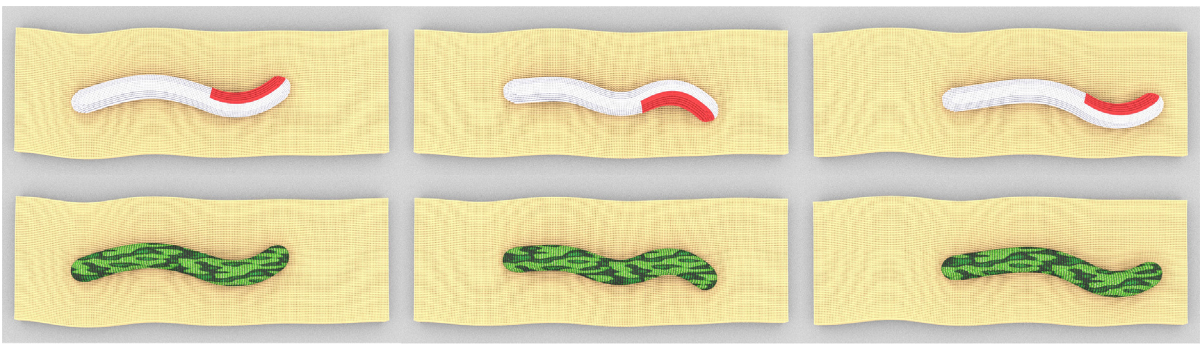

Fig. 11. Top view of snake crawling simulation in Fig. 10.

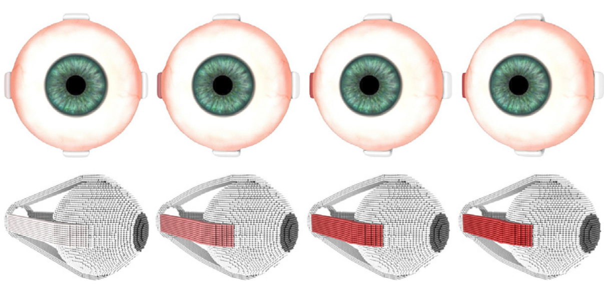

Fig. 12. Muscle contraction moves the eyeball laterally. The Young's modulus is $E = 1 \times 10^5$ Pa. The activation length is set to $c_l = 0.5$.

and isotropic elastic models developed in this study. This nuanced representation allowed us to consider the eyeball as an isotropic elastic object, whilst the four rectus muscles (superior, inferior, lateral, and medial) were represented using our anisotropic elastic model.

Our initial experiments focused on lateral eye movement, as shown in Fig. 12, with muscle activation denoted by a red color code. We gradually increase the activation of the right muscle, shrink the muscle, and then cause eye movements. The model successfully simulated the eye's gaze shifting to the right, providing an improved and accurate depiction of the subtle muscular changes involved.

In a subsequent series of experiments, we manipulated all four rectus muscles to simulate the complex motion of eyeball rolling (Fig. 13). We control the sequential contraction of four muscles to move the gaze in any direction. This nuanced and careful orchestration of the eye's musculature delivered a smooth, realistic rolling motion of the eyeball. We also integrated our detailed ocular structure model into a comprehensive human figure to observe the impact of our simulations in a more holistic and contextually relevant scenario. The result was a more sophisticated and life-like visual portrayal compared to traditional eye movement simulations.

This approach signifies a measured advance in the field, yielding more precise and biologically accurate simulations of eye movement. While this represents a restricted scope of innovation, it holds promise for applications in biological research, medical visualization, animation, and special effects where such meticulous detail can provide added value.

7. Conclusion

In this paper, we have presented a particle-based SPH framework for simulating hyperelastic materials with anisotropic stiffness models. Our approach combines an implicit divergence-free SPH solver with particle-based deformation gradient computation and various elastic energy functions to achieve incompressible elastic simulations. By incorporating anisotropic energy functions constructed from the extrapolation of Cauchy–Green invariants and integrating activation and contraction coefficients, our method effectively represents elastic objects with varying mechanical properties across different directions and can be employed to mimic muscle contractions.

Our framework addresses the current gap in anisotropic elastic simulation studies for particle-based techniques. The experiments conducted in this study demonstrate the effectiveness of our approach in providing realistic simulations for a wide range of animal and human body movements, highlighting its potential for diverse applications in computer graphics, biomechanics, and material science.

However, our method does have certain limitations. Specifically, it struggles with the simulation of extreme squeezing and stretching in highly rigid elastic bodies. Although the combination of Neo-Hookean energy functions and divergence-free SPH computation provides a degree of stability, our method is unable to handle arbitrary deformation in these cases. The particle system becomes unstable and may even explode when particles are too far apart from each other under high Young's modulus conditions. This issue arises from the fixed initial relative positions and neighbor relationships between SPH particles, which generate numerical instability when particles are too distant from one

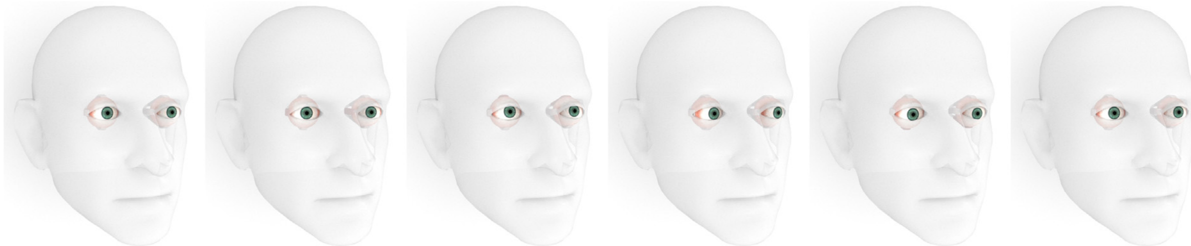

Fig. 13. The sequential contraction of the four muscles results in a complete rotation of the eyeball.

another, particularly when the Young's modulus is high. Moving forward, we plan to explore techniques to implicitly manage extremely rigid elastic solids and enhance the stability of our method, further expanding its applicability to an even broader range of simulations.

In future work, we intend to explore the integration of our particle-based framework with other simulation techniques to create more complex and detailed scenes. Furthermore, we aim to optimize our method for large-scale simulations and real-time applications. We plan to investigate the application of our approach to a broader range of anisotropic materials, enabling more accurate and realistic simulations across various domains.

CRediT authorship contribution statement

Tiancheng Wang: Conceptualization, Methodology. **Yanrui Xu:** Methodology, Writing. **Ruolan Li:** Software, Rendering. **Haoping Wang:** Software, Validation. **Yuege Xiong:** Rendering. **Xiaokun Wang:** Conceptualization, Reviewing and editing.

Declaration of competing interest

The authors declare that they have no known competing financial interests or personal relationships that could have appeared to influence the work reported in this paper.

Data availability

The data that has been used is confidential.

Acknowledgments

This research was founded by:
1. Natural Science Foundation of China (No. 62376025).
2. Horizon 2020-Marie Skłodowska-Curie Action-Individual Fellowships (No. 895941).
3. National Key Research and Development Program of China (No. 2022ZD0118001).
4. Guangdong Basic and Applied Basic Research Foundation (Nos. 2021A1515012285, 2022A1515110350, 2023A1515030177).
5. China Scholarship Council (No. 202206460051).

References

[1] Xiao X, Zhao S, Meng Y, Soghier L, Zhang X, Hahn J. A physics-based virtual reality simulation framework for neonatal endotracheal intubation. In: 2020 IEEE conference on virtual reality and 3D user interfaces. IEEE; 2020, p. 557–65. http://dx.doi.org/10.1109/VR46266.2020.00077.

[2] Lipson H. Challenges and opportunities for design, simulation, and fabrication of soft robots. Soft Robot 2014;1(1):21–7. http://dx.doi.org/10.1089/soro.2013.0007.

[3] Basan M, Prost J, Joanny J-F, Elgeti J. Dissipative particle dynamics simulations for biological tissues: Rheology and competition. Phys Biol 2011;8(2):026014. http://dx.doi.org/10.1088/1478-3975/8/2/026014.

[4] Sifakis E, Barbic J. FEM simulation of 3D deformable solids: A practitioner's guide to theory, discretization and model reduction. In: ACM SIGGRAPH 2012 courses. 2012, http://dx.doi.org/10.1145/2343483.2343501.

[5] Peer A, Gissler C, Band S, Teschner M. An implicit SPH formulation for incompressible linearly elastic solids. Comput Graph Forum 2018;37(6):135–48. http://dx.doi.org/10.1111/cgf.13317.

[6] Koschier D, Bender J, Solenthaler B, Teschner M. Smoothed particle hydrodynamics techniques for the physics based simulation of fluids and solids. 2020, CoRR, arXiv:2009.06944.

[7] Koschier D, Bender J, Solenthaler B, Teschner M. A survey on SPH methods in computer graphics. In: Computer graphics forum. Vol. 41. No. 2. Wiley Online Library; 2022, p. 737–60. http://dx.doi.org/10.1111/cgf.14508.

[8] Becker M, Ihmsen M, Teschner M. Corotated SPH for deformable solids. In: Proceedings of the fifth Eurographics conference on natural phenomena. 2009, p. 27–34. http://dx.doi.org/10.5555/2381692.2381696.

[9] Kim T, De Goes F, Iben H. Anisotropic elasticity for inversion-safety and element rehabilitation. ACM Trans Graph 2019;38(4). http://dx.doi.org/10.1145/3306346.3323014.

[10] Liu T, Bouaziz S, Kavan L. Quasi-newton methods for real-time simulation of hyperelastic materials. ACM Trans Graph (TOG) 2017;36(3):1–16. http://dx.doi.org/10.1145/3072959.2990496.

[11] Wang X, Wang T, Wang J, Xu Y, Ban X, Huang H, et al. Implicit smoothed particle hydrodynamics model for simulating incompressible fluid-elastic coupling. Comput Anim Virt Worlds 2023;e2146. http://dx.doi.org/10.1002/cav.2146.

[12] Kim T, Eberle D. Dynamic deformables: Implementation and production practicalities. In: ACM SIGGRAPH 2020 courses. 2020, p. 1–182. http://dx.doi.org/10.1145/3388769.3407490.

[13] Nealen A, Müller M, Keiser R, Boxerman E, Carlson M. Physically based deformable models in computer graphics. Comput Graph Forum 2006;25(4):809–36. http://dx.doi.org/10.1111/j.1467-8659.2006.01000.x.

[14] Bridson R, Fedkiw R, Anderson J. Robust treatment of collisions, contact and friction for cloth animation. In: Proceedings of the 29th annual conference on computer graphics and interactive techniques. Association for Computing Machinery; 2002, p. 594–603. http://dx.doi.org/10.1145/566570.566623.

[15] Teschner M, Heidelberger B, Muller M, Gross M. A versatile and robust model for geometrically complex deformable solids. In: Proceedings computer graphics international, 2004. 2004, p. 312–9. http://dx.doi.org/10.1109/CGI.2004.1309227.

[16] Selle A, Lentine M, Fedkiw R. A mass spring model for hair simulation. In: ACM SIGGRAPH 2008 papers. 2008, p. 1–11. http://dx.doi.org/10.1145/1399504.1360663.

[17] Liu T, Bargteil AW, O'Brien JF, Kavan L. Fast simulation of mass-spring systems. ACM Trans Graph 2013;32(6). http://dx.doi.org/10.1145/2508363.2508406.

[18] Becker M, Teschner M. Weakly compressible SPH for free surface flows. In: Proceedings of the 2007 ACM SIGGRAPH/Eurographics symposium on computer animation. 2007, p. 209–17. http://dx.doi.org/10.5555/1272690.1272719.

[19] Bender J, Koschier D. Divergence-free smoothed particle hydrodynamics. In: Proceedings of the 14th ACM SIGGRAPH / Eurographics symposium on computer animation. 2015, p. 147–55. http://dx.doi.org/10.1145/2786784.2786796.

[20] Akinci N, Ihmsen M, Akinci G, Solenthaler B, Teschner M. Versatile rigid-fluid coupling for incompressible SPH. ACM Trans Graph 2012;31(4). http://dx.doi.org/10.1145/2185520.2185558.

[21] Monaghan JJ. Smoothed particle hydrodynamics. Ann Rev Astron Astrophys 1992;30(1):543–74. http://dx.doi.org/10.1146/annurev.aa.30.090192.002551.

[22] Müller M, Keiser R, Nealen A, Pauly M, Gross M, Alexa M. Point based animation of elastic, plastic and melting objects. In: Proceedings of the 2004 ACM SIGGRAPH/Eurographics symposium on computer animation. 2004, p. 141–51. http://dx.doi.org/10.1145/1028523.1028542.

[23] Zhou Y, Lun Z, Kalogerakis E, Wang R. Implicit integration for particle-based simulation of elasto-plastic solids. Comput Graph Forum 2013;32(7):215–23. http://dx.doi.org/10.1111/cgf.12229.

[24] Gissler C, Peer A, Band S, Bender J, Teschner M. Interlinked SPH pressure solvers for strong fluid-rigid coupling. ACM Trans Graph 2019;38(1). http://dx.doi.org/10.1145/3284980.

[25] Gissler C, Henne A, Band S, Peer A, Teschner M. An implicit compressible SPH solver for snow simulation. ACM Trans Graph 2020;39(4). http://dx.doi.org/10.1145/3386569.3392431.

[26] Kugelstadt T, Bender J, Fernández-Fernández JA, Jeske SR, Löschner F, Longva A. Fast corotated elastic SPH solids with implicit zero-energy mode control. Proc ACM Comput Graph Interact Tech 2021;4(3). http://dx.doi.org/10.1145/3480142.

[27] Bargteil AW, Wojtan C, Hodgins JK, Turk G. A finite element method for animating large viscoplastic flow. In: ACM SIGGRAPH 2007 papers. 2007, http://dx.doi.org/10.1145/1275808.1276397, 16–es.

[28] Kharevych L, Mullen P, Owhadi H, Desbrun M. Numerical coarsening of inhomogeneous elastic materials. ACM Trans Graph 2009;28(3). http://dx.doi.org/10.1145/1531326.1531357.

[29] Bargteil AW, Cohen E. Animation of deformable bodies with quadratic Bézier finite elements. ACM Trans Graph 2014;33(3). http://dx.doi.org/10.1145/2567943.

[30] Xu H, Sin F, Zhu Y, Barbič J. Nonlinear material design using principal stretches. ACM Trans Graph 2015;34(4):1–11. http://dx.doi.org/10.1145/2766917.

[31] Smith B, Goes FD, Kim T. Stable neo-hookean flesh simulation. ACM Trans Graph 2018;37(2):1–15. http://dx.doi.org/10.1145/3180491.

[32] Kugelstadt T, Koschier D, Bender J. Fast corotated FEM using operator splitting. Comput Graph Forum 2018;37(8):149–60. http://dx.doi.org/10.1111/cgf.13520.

[33] Smith B, Goes FD, Kim T. Analytic eigensystems for isotropic distortion energies. ACM Trans Graph 2019;38(1):1–15. http://dx.doi.org/10.1145/3241041.

[34] Kim T. A finite element formulation of Baraff-Witkin cloth. In: Computer graphics forum. Vol. 39. No. 8. Wiley Online Library; 2020, p. 171–9. http://dx.doi.org/10.1111/cgf.14111.

[35] Stomakhin A, Schroeder C, Chai L, Teran J, Selle A. A material point method for snow simulation. ACM Trans Graph 2013;32(4). http://dx.doi.org/10.1145/2461912.2461948.

[36] Jiang C, Schroeder C, Selle A, Teran J, Stomakhin A. The affine particle-in-cell method. ACM Trans Graph 2015;34(4). http://dx.doi.org/10.1145/2766996.

[37] Hu Y, Fang Y, Ge Z, Qu Z, Zhu Y, Pradhana A, et al. A moving least squares material point method with displacement discontinuity and two-way rigid body coupling. ACM Trans Graph 2018;37(4). http://dx.doi.org/10.1145/3197517.3201293.

[38] Daviet G, Bertails-Descoubes F. A semi-implicit material point method for the continuum simulation of granular materials. ACM Trans Graph 2016;35(4). http://dx.doi.org/10.1145/2897824.2925877.

[39] Jiang C, Gast T, Teran J. Anisotropic elastoplasticity for cloth, knit and hair frictional contact. ACM Trans Graph 2017;36(4). http://dx.doi.org/10.1145/3072959.3073623.

[40] Schreck C, Wojtan C. A practical method for animating anisotropic elasto-plastic materials. Comput Graph Forum 2020;39(2):89–99. http://dx.doi.org/10.1111/cgf.13914.